Tuning the Interfacial Energetics in WO 3 /WO 3 and WO 3 /TiO 2 Heterojunctions by Nanostructure Morphological Engineering

Valentin Diez-Cabanes, Ángel Morales-García, Francesc Illas, Mariachiara Pastore

Tuning the Interfacial Energetics in WO_3/WO_3 and WO_3/TiO_2 Heterojunctions by Nanostructure Morphological Engineering

Valentin Diez-Cabanes,[1,*] *Ángel Morales-García,*[2,*] *Francesc Illas,*[2] *Mariachiara Pastore*[1,*]

[1] Université de Lorraine & CNRS, Laboratoire de Physique et Chimie Théoriques (LPCT), UMR 7019, F-54000, Nancy, France

[2] Departament de Ciència de Materials i Química Física & Institut de Química Teòrica i Computacional (IQTCUB), Universitat de Barcelona, c/Martí i Franqués 1-11, 08028 Barcelona, Spain

*Authors to whom correspondence should be addressed: valentin.diez-cabanes@univ-lorraine.fr; angel.morales@ub.edu; mariachiara.pastore@univ-lorraine.fr

ABSTRACT

Nowadays, semiconducting heterojunction-based devices exhibit the best photocatalytic performance, with transition metal oxides like tungsten (WO_3) and titanium (TiO_2) being the workhorse materials employed in these composites. Contrary to their bulk counterparts, WO_3 and TiO_2 nanostructures offer a huge versatility because their opto-electronic properties (*i.e.*, energy levels) can be tuned by modifying their size, morphology, and composition, thus being, in principle, able to optimize the electron/hole injection barriers inside the device. However, this approach requires a deep fundamental knowledge of their structure-property relationships, extremely difficult to access from experiments. In this context, we employed state-of-art theoretical methods to determine the size and morphology dependency of the energetic alignment in WO_3/WO_3 and TiO_2/WO_3 nanostructure heterojunctions. Our results demonstrated that any type of alignment can be achieved by the proper choice of the nanostructures involved in the junction, while setting important rules for the design of efficient multi-component devices.

TOC GRAPHICS

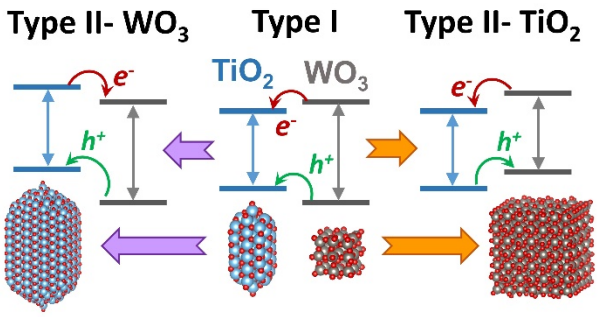

Heterojunction formed by two or more semiconducting materials constitute the most common architecture employed in photocatalysis. This is due to several existing advantages with respect to the single semiconductor devices, such as the possibility to monitor the surface exposed to reaction, the enhancement of the visible light absorption and more importantly the possible reduction of the charge recombination rate of the photogenerated carriers via an efficient charge separation at the junction interface.[1–3] Notably, the band alignment of the materials integrating the junction will ultimately determine the efficiency of this charge separation process and will drive the functionality of the system, as it is exemplified in Scheme 1.[4]

As a matter of fact, tungsten trioxide[5,6] (WO_3) and titanium dioxide[7] (TiO_2) are among the most common semiconductors employed in photocatalysis due to their strong light absorption, low cost production and high stability. In particular, the heterojunctions formed by these two catalysts or combined in form of ternary alloys[8] are widely used in the degradation of organic pollutants.[9–11] Indeed, an improved photocatalytic activity of these composites with respect to single TiO_2[12–14] or WO_3[15–17] devices has been reported and attributed to an efficient charge transfer between the two materials, where WO_3 and TiO_2 act as reservoirs of the photogenerated holes and electrons, respectively.[18,19] Alternatively, one can also form heterojunctions with different polymorphs from the same material. The prototype example of this type of composites is the commercial P25 (Degussa) photocatalyst which combines anatase and rutile TiO_2 nanoparticles (NPs) and it has been largely investigated during the last decades,[20,21] especially with a focus on the band alignment between both TiO_2 phases.[22–24] Unfortunately, this is not the case for WO_3 based composites, for which only few works[25–27] have been reported till the date, despite the large variety of phases and morphologies of WO_3 nanomaterials.[28–30] In practice, most heterojunctions are formed by bulk-like semiconductors, thus leading to different types of band alignments and functionalities for a given

combination of materials. In this regard one must point out that, relying, for instance, on facet engineering, nanostructures of different morphologies and sizes can be experimentally obtained.[31] This implies that one can improve the performance of the device tuning the interfacial energetics of the junction by suitably modifying the electronic structure of the nanomaterials conforming the junction via quantum confinement and/or surface termination effects.[32] Nevertheless, to achieve such a precise control on the junction energetic barriers, an accurate estimation of the energy levels of the materials, together with a deep knowledge of their evolution with respect to the size and the morphology, becomes unavoidable.[33] In this context, we recently developed a high accurate theoretical approach, capable to reliably estimate the electronic properties of realistic-sized WO_3 NPs for all representative morphologies experimentally reported.[34] In addition, some of us recently investigated the size dependency of the energetics of TiO_2 anatase/rutile NP junctions on the basis of a first-principles approach, predicting that the most common band alignment found for these composites (Type II-anatase) can be modified by decreasing the TiO_2 NPs diameter below ~15 nm.[35] Inspired by this idea, we make use of this strategy to determine the junction energetics for a given combination of WO_3/WO_3 and WO_3/TiO_2 NPs involving different sizes and morphologies. We will show that some novel rules to boost the functionality of these heterojunctions can be derived and that the key issue is opportunely playing with the morphology of the nanostructures composing the junction. It is noteworthy to highlight that here we do not explicitly model the interfaces between the materials of the junction, assuming that the relative energy levels alignment is not significantly different from that obtained for the two isolated nanostructures. This is a consequence of the relatively small number of atoms in the interfacial region compared to that of the constituent nanoparticles. The soundness of this approximation for the considered systems has been verified in Ref 18., where theoretical calculations on the isolated WO_3 and TiO_2 bulk phases

were able to properly reproduce the experimental energetic alignment observed in TiO_2/WO_3 composites. Moreover, atomistic modelling of heterojunctions can be extremely challenging because of the problem of finding the proper DFT functional for different systems, of physically building the junction (choice of the surface termination, strain etc…), as well as of handling with possible size confinement effects in the case of nanostructures. A more rigorous approach, as the one used by Pacchioni and co-workers in Refs. 36–39 to study the energetics of multiple junctions, would require the use of explicit models to accurately describe the complexity of the interfacial chemical interactions taking place, but this goes beyond the scope of the present work.

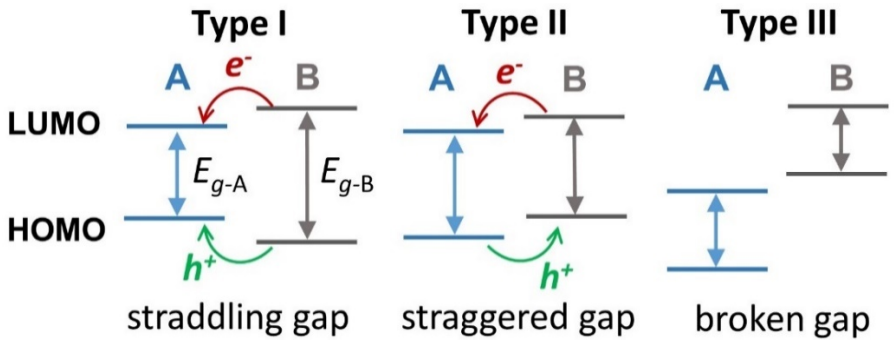

Scheme 1. Representation of the three possible types of alignment for junctions composed of A and B nanomaterials. In the following we will use the terminology Type I-A or Type II-A to specify which material (A in this case) is acting as the electron reservoir of the junction.

The complete set of NPs investigated in this work (Figure 1) involves cubic, rectangular prismoid and spherical monoclinic WO_3 NPs, nanosheet and nanowire hexagonal WO_3 NPs, and anatase and rutile TiO_2 NPs. Further details about the construction of these nanostructures are provided in detail in refs. 34 and 35 for WO_3 and TiO_2 NPs, respectively. The electronic structure of these systems was calculated by performing all electron relativistic Density Functional Theory (DFT)

calculations employing the Perdew-Burke-Ernzerhof (PBE) functional.[40] Then, the band edges of the NPs have been obtained following the procedure described in the Supporting Information (SI). Here it suffices to point out that these do not correspond to the raw PBE Kohn-Sham orbital energies, as they involve extrapolation from *GW* or suitable hybrid functionals results, in such a way that periodic calculations for the bulk phases approach the experimental values and reproduces the experimental band gap (see section S2 of the SI). In the following we will refer to the frontier orbital energies as corrected HOMO/LUMO (denoted as c-HOMO and c-LUMO, respectively) to emphasize that these do not correspond to the Kohn-Sham orbital energies.

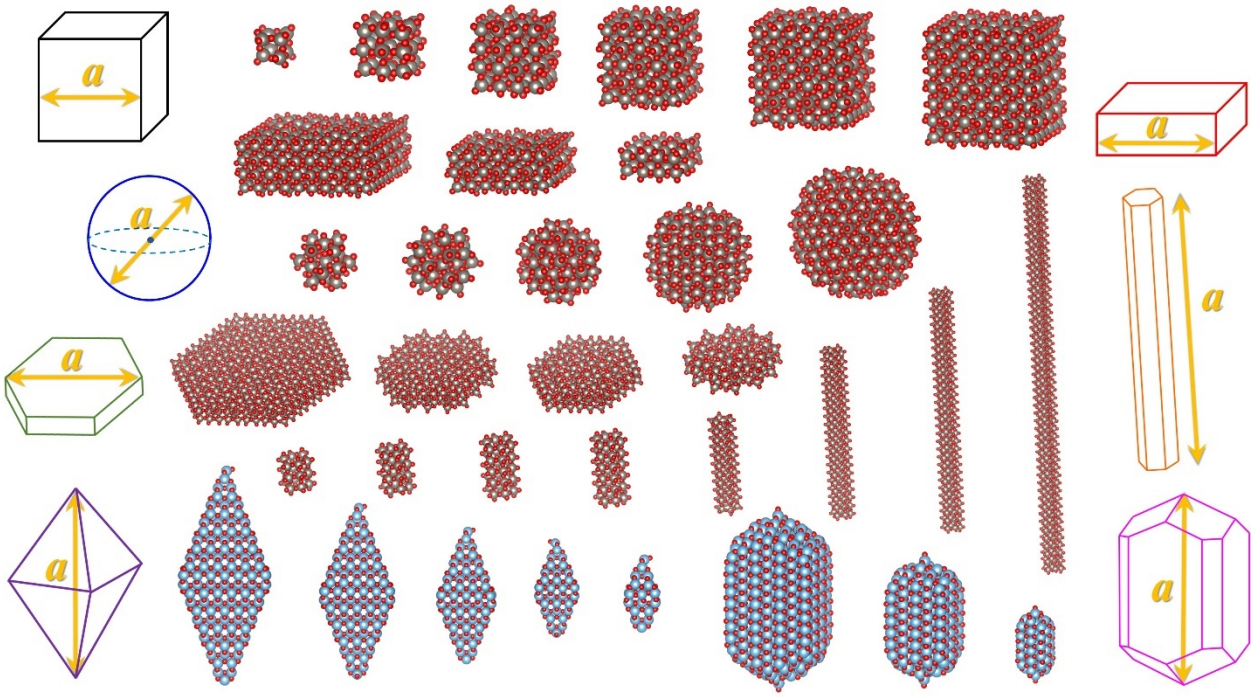

Figure 1. The full set of WO_3 and TiO_2 NPs investigated in this work (from the top to the bottom and from the left to the right): n=8, 27, 64, 125, 216, and 343 cubic $(WO_3)_n$ particles; rectangular-shaped $(WO_3)_n$ particles with n=400, 147, and 32; spherical-shaped $(WO_3)_n$ particles with n=19, 32, 57, 80, 147 and 281; hexagonal nanosheet $(WO_3)_n$ particles with n=420, 180, 144 and 84; cuboid nanowires $(WO_3)_n$ particles with n=18, 24, 30, 36, 66, 126, 186 and 306; anatase $(TiO_2)_n$

particles with n=455, 286, 165, 84 and 35; and rutile $(TiO_2)_n$ particles with n=563, 211 and 51. A scheme representing the corresponding characteristic length for each morphology is also shown. Note that the suitability of our length parameters to investigate the size-dependency of the electronic properties of our NPs has been corroborated by analysing their correlation with n, the number of units (see Figure S1). Blue, grey, and red spheres represent Ti, W, and O atoms, respectively.

In a first approximation, the size-dependency of the energetic levels of each NP family has been estimated by applying a modified particle-in-a-box model. In this framework, one assumes that when a finite NP is in the quantum confinement regime, its energy levels (E) follow a $E \propto L^{-\alpha}$ size dependency, where L is the length parameter of the box and α is an exponential term ($E \propto L^{-\alpha}$) spanning from $1<\alpha<2$, obtained by fitting the data against experimental[41] or quantum mechanical[35,42] observables. In our case, the values of α for each NP family have been chosen to get the best compromise between reducing the fitting errors and reaching size-converged values of the estimated of the c-HOMO/c-LUMO energies as described at length in section S1.1 of the SI (Table 1). Interestingly, the size-converged values of E_g for the monoclinic NPs (cubic, rectangular and spherical) lie in a range (2.50-2.76 eV) comparable to the experimental value of the bulk (2.62 eV),[43] similarly to what was reported for TiO_2 NPs.[35] Regarding the band edges, the size-converged c-HOMO/c-LUMO energies (see Figure S2 in SI) overestimate their corresponding experimental valence/conduction band edges by a similar quantity (0.7-1.0 eV taking cubic and anatase NPs as reference for WO_3 and TiO_2 bulk phases, respectively) for both WO_3 and TiO_2 NPs. This allows us to conclude that the employed level of theory is capable to reproduce the relative band alignment of the two materials (WO_3 and TiO_2) investigated here.

Table 1. Fitting parameters for the $E \propto a^{-\alpha}$ correlations of each NP family as plotted in Figures S2 and S3. The values reported in parenthesis correspond to the typical band edge and energy gap energies of the bulk phases which are often reported in the literature.[44,45] Note that, in spite of a relatively large error on the band edges, the band gap estimated from corrected HOMO-LUMO levels nicely approaches the experimental value which is in agreement with the similar error in the band edges commented above.

NP type	α	(c-HOMO)$_\infty$	(c-LUMO)$_\infty$	E_g
cubic	1.4	-8.31 (-7.6)	-5.69 (-5.0)	2.62 (2.6)
rectangular	1	-8.60 (-7.6)	-5.84 (-5.0)	2.76 (2.6)
spherical	1.6	-9.04 (-7.6)	-6.54 (-5.0)	2.50 (2.6)
nanosheet	1	-7.63	-3.91	3.72
nanowire	1	-9.12	-5.59	3.53
anatase	1.35	-8.30 (-7.3)	-4.98 (-4.1)	3.32 (3.2)
rutile	1.35	-7.64	-4.94	2.70 (3.0)

The $E \propto L^{-\alpha}$ fitting plots for all NP morphologies are reported in Figures S2 and S3. Notably, for the spherical WO_3 NPs one can observe that below Ø~3.3 nm, the HOMO is localized on the oxygen surface atoms, whereas above this size it is confined at the NP's core. Clearly, in the small-size regime the c-HOMO energies are independent of the NP diameter, whereas the size dependency is much more pronounced for the larger NPs. From a photocatalytic point of view, highly localized HOMOs such as the ones present in the surface of the small spherical NPs can be detrimental for the charge carrier transport and the overall device performance since they can promote the recombination of the photogenerated holes.[46,47] Similar findings were reported for rutile TiO_2 NPs,[35] for which, however, a larger crossover diameter (~6.9 nm) was identified. The

fitting parameters reported in Table 1 give us access to the evolution of the c-HOMO/c-LUMO energies as a function of the characteristic NP length, as it is represented in Figure 2.

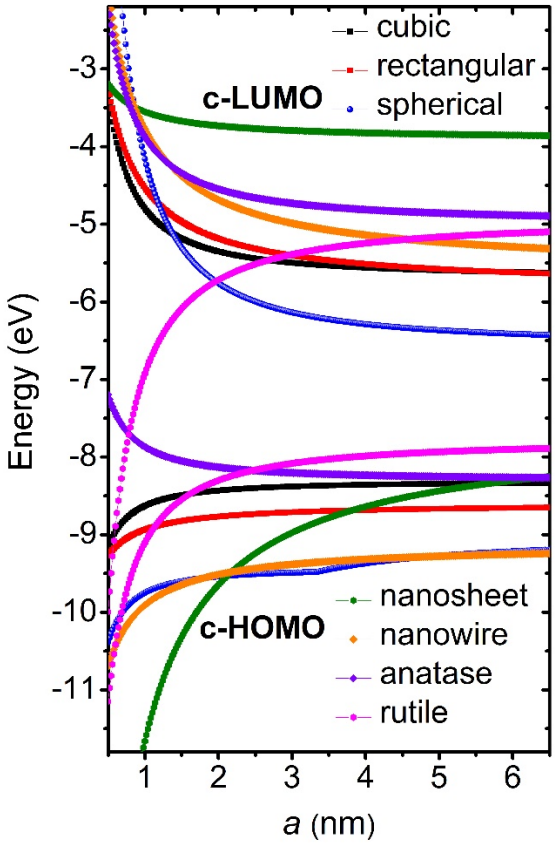

Figure 2. Corrected HOMO and LUMO energies as function of the characteristic length of the WO_3 (monoclinic cubic, rectangular, spherical, and for the hexagonal nanosheets and nanowire) and TiO_2 (anatase and rutile) NPs.

Interestingly, the dependence of the energy levels on the NP size for TiO_2 and WO_3 NPs is completely different: while for anatase/rutile TiO_2 NPs, both c-HOMO and c-LUMO levels down-/up-shift as the NP size increases, the c-HOMO/c-LUMO energies of the WO_3 NPs up-/down-shift by increasing their size. As a result, the band alignment of a given heterojunction can be tuned at will, especially for those NP families whose energetics are particularly sensitive to their size, such

as spherical, nanosheet, and rutile particles. We are now ready to build the energetic maps which will disclose the different types of alignments achievable for a given combination of NPs. The data for heterojunctions formed by two WO_3 NPs of different morphology are plotted in Figure 3, where the range of NP size represented spans from the size of the smallest synthetized WO_3 quantum dot (0.7 nm)[48] to the characteristic size of a NP displaying a bulk-like electronic structure (~10 nm).

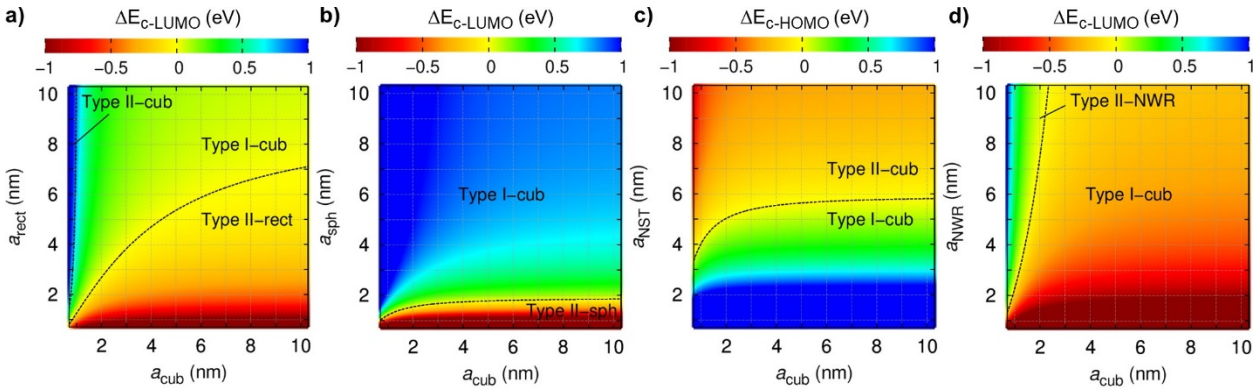

Figure 3. Energy maps for the electron/hole injection barriers as function of the NP characteristic length for the junctions formed by a cubic WO_3 (*x*-axis) and the rest of WO_3 families (*y*-axis) of NPs. Energy scales indicating the difference in c-HOMO/c-LUMO values ($\Delta E_{c\text{-}HOMO/c\text{-}LUMO}$=$E_{c\text{-}HOMO/c\text{-}LUMO}$(*x*-axis)- $E_{c\text{-}HOMO/c\text{-}LUMO}$(*y*-axis)) are presented on the top of the plots. The rest of the WO_3 NP based junction energy maps are collected in Figure S4.

Cubic and rectangular WO_3 NPs possess the largest/smallest c-LUMO/c-HOMO energies for most of particle sizes (see Figure 2) and thus type I alignment dominates their energy maps (see Figure 3 and Figures S4 a-c). Furthermore, in view of their identical atomic structure, their c-LUMO energies remain very close for all range of NP sizes (Figure 2), thus allowing to reverse the flow of electrons very easily by changing the relative size of the two NPs; whereas a change in the hole transport direction is only obtained when employing rather small cubic WO_3 NPs (< 1 nm) in the

heterojunction (Figure 3a). Spherical WO_3 NPs display the deepest c-HOMO and c-LUMO energies for the medium and large size regime but, when moving to small NPs the c-LUMO levels start to upshift considerably (see Figure 2), yielding to a change in the electron transport direction (Figure 3b and Figures S4 a, c and d) upon going below a certain diameter (1.8, 2, 1 and 1.7 nm for cubic, rectangular, nanosheet and nanowire NPs). Concerning the WO_3 nanosheet NPs, they exhibit the shallowest c-LUMO levels for all NP sizes, whereas their c-HOMO energies are sensibly downshifted when reducing the NP size. These features result in a reversion of the hole transport direction when moving from medium to large size nanosheet NPs (5.7, 4, 2.6 and 2.5 nm for cubic, rectangular, spherical and nanowire NPs) for all possible junction combinations (see Figures 3c and S4-b, c and e). Finally, due to the relatively low c-LUMO levels and deep c-HOMO energies, nanowire nanostructures exhibit a change in the electron flow direction only when they are coupled to small NPs of the other families (see Figure 3d).

In a second step, we have investigated the type of alignment exhibited by heterojunctions composed by either anatase or rutile TiO_2 NPs and the distinct WO_3 NP morphologies. The most representative maps for these heterojunctions are collected in Figure 4.

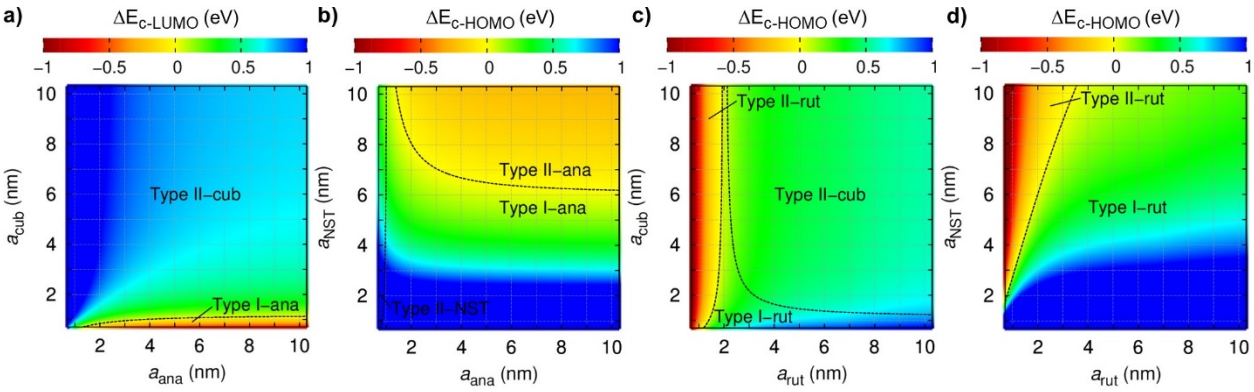

Figure 4. Energy maps for the electron/hole injection barriers as function of the NP characteristic length for the junctions formed by anatase (a- and b-) and rutile (c- and d-) TiO_2 NPs (x-axis) with

cubic and nanosheet WO_3 NPs (*y*-axis). The rest of the TiO_2/WO_3 junction energy maps are presented in Figure S5.

Anatase energy levels were found to be lower in energy with respect to those of WO_3 nanostructures for a wide range of NP sizes, thus making the Type II-WO_3 alignment the most common one for these junctions. Indeed, we found only two exceptions to this type of alignment: a change in the electron flow direction when coupled to small cubic, rectangular, spherical and nanowire NPs (see Figure 4a and Figures S5a-c), and in the hole transport, if combined with small-medium nanosheets (Figure 4b). On the other hand, rutile NPs coupled to WO_3 exhibit a larger capability to reach different type of alignments when compared to coupling anatase and WO_3 NPs, since their energy levels are much more sensitive to the NP size. For instance, when anatase is assembled with cubic, rectangular, spherical or nanowire WO_3 NPs, three distinct types of alignment can be obtained: Type I-rutile formed by small NPs of both materials; Type II-rutile by increasing the size of the WO_3 NPs, and Type II-WO_3 by employing larger rutile NPs in the heterojunction (see Figure 4c and Figures S5d-f). Strikingly, rutile-nanosheet composites follow a different behavior with respect to the rest of nanosheet based junctions, since the change in hole flow direction is more influenced by the size of the rutile NP than the one of the nanosheet.

To summarize, this work presents for the first time a systematic theoretical study of the size-dependency of the energetic alignments reached in junctions formed by different arrangements of WO_3/WO_3 and TiO_2/WO_3 nanostructures. For the former composites, cubic and rectangular NPs were shown especially suitable for obtaining Type I alignments, whereas modifying the size from small-to-medium and medium-to-large of spherical and hexagonal particles was found to be a convenient approach to tune the electron and hole transport directions respectively, thus enabling to access to district Type II alignments. In the case of TiO_2/WO_3 junctions, while anatase/WO_3

particles show a dominant Type II-WO_3 alignment (with the exception of hexagonal NPs), rutile/WO_3 NPs exhibit much more flexibility in terms of energetics, being the rutile particle diameter the dominant factor dictating the change in the type of alignment. Overall, our results clearly demonstrate that it is possible to obtain the desired band alignment in WO_3/TiO_2 interface via morphological engineering of the nanostructures composing the junction. We hope this work will encourage the scientific community to put more efforts in the synthesis of nanostructures with finely controlled geometry which indeed, can be successfully exploited for photocatalytic purposes.

ASSOCIATED CONTENT

Supporting Information

The Supporting Information is available free of charge on the ACS Publications website. Tests for different methodologies, plots $L \propto n$ and $E \propto L^{-\alpha}$ correlations, and energetic maps for the rest of WO_3/ WO_3 and TiO_2/WO_3 heterojunctions.

AUTHOR INFORMATION

Corresponding Authors

Valentin Diez-Cabanes- *Université de Lorraine & CNRS, Laboratoire de Physique et Chimie Théoriques (LPCT), UMR 7019, F-54000, Nancy, France* ORCID: https://orcid.org/0000-0002-6234-2749. Email: valentin.diez-cabanes@univ-lorraine.fr

Ángel Morales-García- *Departament de Ciència de Materials i Química Física & Institut de Química Teòrica i Computacional (IQTUB), Universitat de Barcelona, c/Martí i Franqués 1-11,*

08028 Barcelona, Spain ORCID: https://orcid.org/0000-0003-0491-1234. Email: angel.morales@ub.edu

Mariachiara Pastore- *Université de Lorraine & CNRS, Laboratoire de Physique et Chimie Théoriques (LPCT), UMR 7019, F-54000, Nancy, France*. ORCID: https://orcid.org/0000-0003-4793-1964. Email: mariachiara.pastore@univ-lorraine.fr

Authors

Francesc Illas- *Departament de Ciència de Materials i Química Física & Institut de Química Teòrica i Computacional (IQTUB), Universitat de Barcelona, c/Martí i Franqués 1-11, 08028 Barcelona, Spain* ORCID: https://orcid.org/0000-0003-2104-6123.

Notes

The authors declare no competing financial interest.

ACKNOWLEDGMENT

V.D.-C. and M. P. acknowledge the COMETE project (COnception in silico de Matériaux pour l'EnvironnemenT et l'Energie), which is co-funded by the European Union under the program 'FEDER-FSE Lorraine et Massif des Vosges 2014-2020; for the financial support. The work carried out at the Universitat de Barcelona has been supported by the Spanish MICIUN RTI2018-095460-B-I00 and María de Maeztu MDM-2017-0767 grants and, in part, to COST Action CA18234. A.M.-G. is thankful to the Juan de la Cierva Incorporación Programme grant IJCI-2017-31979. Computational resources were provided by the LPCT local clusters, the mésocentre EXPLOR of Université de Lorraine (Project 2018CPMXX0602), the Très Grand Centre de Calcul

du CEA (TGCC) facilities, Red Española de Supercomputacion (RES) (grant QS-2020-2-0008), and the HPC-Europa3 Transnational Access programme (project number HPC17N1MY8).

REFERENCES

(1) Wang, H.; Zhang, L.; Chen, Z.; Hu, J.; Li, S.; Wang, Z.; Liu, J.; Wang, X. Semiconductor Heterojunction Photocatalysts: Design, Construction, and Photocatalytic Performances. *Chem. Soc. Rev.* **2014**, *43*, 5234–5244.

(2) Marschall, R. Semiconductor Composites: Strategies for Enhancing Charge Carrier Separation to Improve Photocatalytic Activity. *Adv. Funct. Mater.* **2014**, *24*, 2421–2440.

(3) Moniz, S. J. A.; Shevlin, S. A.; Martin, D. J.; Guo, Z. X.; Tang, J. Visible-Light Driven Heterojunction Photocatalysts for Water Splitting-a Critical Review. *Energy Environ. Sci.* **2015**, *8*, 731–759.

(4) Cahen, D.; Kahn, A. Electron Energetics at Surfaces and Interfaces: Concepts and Experiments. *Adv. Mater.* **2003**, *15*, 271–277.

(5) Huang, Z. F.; Song, J.; Pan, L.; Zhang, X.; Wang, L.; Zou, J. J. Tungsten Oxides for Photocatalysis, Electrochemistry, and Phototherapy. *Adv. Mater.* **2015**, *27*, 5309–5327.

(6) Zheng, G.; Wang, J.; Liu, H.; Murugadoss, V.; Zu, G.; Che, H.; Lai, C.; Li, H.; Ding, T.; Gao, Q.; Guo, Z. Tungsten Oxide Nanostructures and Nanocomposites for Photoelectrochemical Water Splitting. *Nanoscale* **2019**, *11*, 18968–18994.

(7) Nakata, K.; Fujishima, A. TiO2 Photocatalysis: Design and Applications. *J. Photochem.*

Photobiol. C Photochem. Rev. **2012**, *13*, 169–189.

(8) Pinedo-Escobar, J. A.; Fan, J.; Moctezuma, E.; Gomez-Solís, C. Nanoparticulate Double Heterojunction Photocatalysts Comprising the Degradation of Methyl Orange under near UV and Visible Light. *ACS Omega* **2021**, *6*, 11840–11848.

(9) Ramos-Delgado, N. A.; Gracia-Pinilla, M. A.; Maya-Treviño, L.; Hinojosa-Reyes, L.; Guzman-Mar, J. L.; Hernández-Ramírez, A. Solar Photocatalytic Activity of TiO2 Modified with WO3 on the Degradation of an Organophosphorus Pesticide. *J. Hazard. Mater.* **2013**, *263*, 36–44.

(10) Ke, D.; Liu, H.; Peng, T.; Liu, X.; Dai, K. Preparation and Photocatalytic Activity of WO3/TiO2 Nanocomposite Particles. *Mater. Lett.* **2008**, *62*, 447–450.

(11) Liu, H.; Guo, W.; Li, Y.; He, S.; He, C. Photocatalytic Degradation of Sixteen Organic Dyes by TiO2/WO3-Coated Magnetic Nanoparticles under Simulated Visible Light and Solar Light. *J. Environ. Chem. Eng.* **2018**, *6*, 59–67.

(12) Liu, Y.; Zeng, X.; Easton, C. D.; Li, Q.; Xia, Y.; Yin, Y.; Hu, X.; Hu, J.; Xia, D.; McCarthy, D. T.; Deletic, A.; Sun, C.; Yu, J.; Zhang, X. An: In Situ Assembled WO3-TiO2 Vertical Heterojunction for Enhanced Z-Scheme Photocatalytic Activity. *Nanoscale* **2020**, *12*, 8775–8784.

(13) Yan, M.; Li, G.; Guo, C.; Guo, W.; Ding, D.; Zhang, S.; Liu, S. WO3-x Sensitized TiO2 Spheres with Full-Spectrum-Driven Photocatalytic Activities from UV to near Infrared. *Nanoscale* **2016**, *8*, 17828–17835.

(14) Tahir, M. B.; Farman, S.; Rafique, M.; Shakil, M.; Khan, M. I.; Ijaz, M.; Mubeen, I.; Ashraf,

M.; Nadeem Riaz, K. Photocatalytic Performance of Hybrid WO3/TiO2 Nanomaterials for the Degradation of Methylene Blue under Visible Light Irradiation. *Int. J. Environ. Anal. Chem.* **2019**, *00*, 1–13.

(15) Wang, C.; Zhang, X.; Yuan, B.; Wang, Y.; Sun, P.; Wang, D.; Wei, Y.; YichunLiu. Multi-Heterojunction Photocatalysts Based on WO3 Nanorods: Structural Design and Optimization for Enhanced Photocatalytic Activity under Visible Light. *Chem. Eng. J.* **2014**, *231*, 29–37.

(16) Ohashi, T.; Sugimoto, T.; Sako, K.; Hayakawa, S.; Katagiri, K.; Inumaru, K. Enhanced Photocatalytic Activity of Pt/WO3 Photocatalyst Combined with TiO2 Nanoparticles by Polyelectrolyte-Mediated Electrostatic Adsorption. *Catal. Sci. Technol.* **2015**, *5*, 1163–1168.

(17) Nagy, D.; Firkala, T.; Drotár, E.; Szegedi, Á.; László, K.; Szilágyi, I. M. Photocatalytic WO3/TiO2 Nanowires: WO3 Polymorphs Influencing the Atomic Layer Deposition of TiO2. *RSC Adv.* **2016**, *6*, 95369–95377.

(18) Sotelo-Vazquez, C.; Quesada-Cabrera, R.; Ling, M.; Scanlon, D. O.; Kafizas, A.; Thakur, P. K.; Lee, T. L.; Taylor, A.; Watson, G. W.; Palgrave, R. G.; et al. Evidence and Effect of Photogenerated Charge Transfer for Enhanced Photocatalysis in WO3/TiO2 Heterojunction Films: A Computational and Experimental Study. *Adv. Funct. Mater.* **2017**, *27*, 1–10.

(19) Iqbal, A.; Kafizas, A.; Sotelo-Vazquez, C.; Wilson, R.; Ling, M.; Taylor, A.; Blackman, C.; Bevan, K.; Parkin, I.; Quesada-Cabrera, R. Charge Transport Phenomena in Heterojunction Photocatalysts : The WO3/TiO2 System as an Archetypical Model. *ACS Appl. Mater. Interfaces* **2021**, *13*, 9781–9793.

(20) Hurum, D. C.; Agrios, A. G.; Gray, K. A.; Rajh, T.; Thurnauer, M. C. Explaining the Enhanced Photocatalytic Activity of Degussa P25 Mixed-Phase TiO2 Using EPR. *J. Phys. Chem. B* **2003**, *107*, 4545–4549.

(21) Ohtani, B.; Prieto-Mahaney, O. O.; Li, D.; Abe, R. What Is Degussa (Evonic) P25? Crystalline Composition Analysis, Reconstruction from Isolated Pure Particles and Photocatalytic Activity Test. *J. Photochem. Photobiol. A Chem.* **2010**, *216*, 179–182.

(22) Scanlon, D. O.; Dunnill, C. W.; Buckeridge, J.; Shevlin, S. A.; Logsdail, A. J.; Woodley, S. M.; Catlow, C. R. A.; Powell, M. J.; Palgrave, R. G.; Parkin, I. P.; et al. Band Alignment of Rutile and Anatase TiO2. *Nat. Mater.* **2013**, *12*, 798–801.

(23) Nosaka, Y.; Nosaka, A. Y. Reconsideration of Intrinsic Band Alignments within Anatase and Rutile TiO2. *J. Phys. Chem. Lett.* **2016**, *7*, 431–434.

(24) Kafizas, A.; Wang, X.; Pendlebury, S. R.; Barnes, P.; Ling, M.; Sotelo-Vazquez, C.; Quesada-Cabrera, R.; Li, C.; Parkin, I. P.; Durrant, J. R. Where Do Photogenerated Holes Go in Anatase:Rutile TiO2? A Transient Absorption Spectroscopy Study of Charge Transfer and Lifetime. *J. Phys. Chem. A* **2016**, *120*, 715–723.

(25) Li, Y.; Tang, Z.; Zhang, J.; Zhang, Z. Fabrication of Vertical Orthorhombic/Hexagonal Tungsten Oxide Phase Junction with High Photocatalytic Performance. *Appl. Catal. B Environ.* **2017**, *207*, 207–217.

(26) Lu, Y.; Zhang, J.; Wang, F.; Chen, X.; Feng, Z.; Li, C. K2SO4-Assisted Hexagonal/Monoclinic WO3 Phase Junction for Efficient Photocatalytic Degradation of RhB. *ACS Appl. Energy Mater.* **2018**, *1*, 2067–2077.

(27) Kang, M.; Liang, J.; Wang, F.; Chen, X.; Lu, Y.; Zhang, J. Structural Design of Hexagonal/Monoclinic WO3 Phase Junction for Photocatalytic Degradation. *Mater. Res. Bull.* **2020**, *121*, 110614.

(28) Zheng, H.; Ou, J. Z.; Strano, M. S.; Kaner, R. B.; Mitchell, A.; Kalantar-Zadeh, K. Nanostructured Tungsten Oxide - Properties, Synthesis, and Applications. *Adv. Funct. Mater.* **2011**, *21*, 2175–2196.

(29) Xie, Y. P.; Liu, G.; Yin, L.; Cheng, H. M. Crystal Facet-Dependent Photocatalytic Oxidation and Reduction Reactivity of Monoclinic WO3 for Solar Energy Conversion. *J. Mater. Chem.* **2012**, *22*, 6746–6751.

(30) Lin, R.; Wan, J.; Xiong, Y.; Wu, K.; Cheong, W. C.; Zhou, G.; Wang, D.; Peng, Q.; Chen, C.; Li, Y. Quantitative Study of Charge Carrier Dynamics in Well-Defined WO3 Nanowires and Nanosheets: Insight into the Crystal Facet Effect in Photocatalysis. *J. Am. Chem. Soc.* **2018**, *140*, 9078–9082.

(31) Wang, S.; Liu, G.; Wang, L. Crystal Facet Engineering of Photoelectrodes for Photoelectrochemical Water Splitting. *Chem. Rev.* **2019**, *119*, 5192–5247.

(32) Diez-Cabanes, V.; Pastore, M. Morphological Engineering of Inorganic Semiconductor VIS-Light-Driven Nanocatalysts: Experimental and Theoretical Understandings. *J. Phys. Chem. C* **2021**, *125*, 15125–15133.

(33) Morales-García, Á.; Macià Escatllar, A.; Illas, F.; Bromley, S. T. Understanding the Interplay between Size, Morphology and Energy Gap in Photoactive TiO2 Nanoparticles. *Nanoscale* **2019**, *11*, 9032–9041.

(34) Diez-Cabanes, V.; Morales-Garcia, A.; Illas, F.; Pastore, M. Understanding the Structural and Electronic Properties of Photoactive Tungsten Oxide Nanoparticles from Density Functional Theory and GW Approaches. *J. Chem. Theory Comput.* **2021**, *17*, 3462–3470.

(35) Ko, K. C.; Bromley, S. T.; Lee, J. Y.; Illas, F. Size-Dependent Level Alignment between Rutile and Anatase TiO2 Nanoparticles: Implications for Photocatalysis. *J. Phys. Chem. Lett.* **2017**, *8*, 5593–5598.

(36) Cerrato, E.; Gionco, C.; Paganini, M. C.; Giamello, E.; Albanese, E.; Pacchioni, G. Origin of Visible Light Photoactivity of the CeO2/ZnO Heterojunction. *ACS Appl. Energy Mater.* **2018**, *1*, 4247–4260.

(37) Di Liberto, G.; Tosoni, S.; Pacchioni, G. Role of Heterojunction in Charge Carrier Separation in Coexposed Anatase (001)-(101) Surfaces. *J. Phys. Chem. Lett.* **2019**, *10*, 2372–2377.

(38) Di Liberto, G.; Cipriano, L. A.; Tosoni, S.; Pacchioni, G. Rational Design of Semiconductor Heterojunctions for Photocatalysis. *Chem. - A Eur. J.* **2021**, *27*, 13306–13317.

(39) Di Liberto, G.; Tosoni, S.; Pacchioni, G. Role of Surface Termination in Forming Type-II Photocatalyst Heterojunctions: The Case of TiO2/BiVO4. *J. Phys. Condens. Matter* **2021**, *33*, 075001.

(40) Perdew, J. P.; Burke, K.; Ernzerhof, M. Generalized Gradient Approximation Made Simple. *Phys. Rev. Lett.* **1996**, *77*, 3865–3868.

(41) Yu, H.; Li, J.; Loomis, R. A.; Wang, L. W.; Buhro, W. E. Two-versus Three-Dimensional Quantum Confinement in Indium Phosphide Wires and Dots. *Nat. Mater.* **2003**, *2*, 517–520.

(42) Fu, H.; Zunger, A. InP Quantum Dots: Electronic Structure, Surface Effects, and the Redshifted Emission. *Phys. Rev. B - Condens. Matter Mater. Phys.* **1997**, *56*, 1496–1508.

(43) Gullapalli, S. K.; Vemuri, R. S.; Ramana, C. V. Structural Transformation Induced Changes in the Optical Properties of Nanocrystalline Tungsten Oxide Thin Films. *Appl. Phys. Lett.* **2010**, *96*, 20–23.

(44) Grätzel, M. Photoelectrochemical Cells. *Nature* **2001**, *414*, 338–344.

(45) Tong, H.; Ouyang, S.; Bi, Y.; Umezawa, N.; Oshikiri, M.; Ye, J. Nano-Photocatalytic Materials: Possibilities and Challenges. *Adv. Mater.* **2012**, *24*, 229–251.

(46) Linsebigler, A. L.; Lu, G.; Yates, J. T. Photocatalysis on TiO2 Surfaces: Principles, Mechanisms, and Selected Results. *Chem. Rev.* **1995**, *95*, 735–758.

(47) Chen, X.; Shen, S.; Guo, L.; Mao, S. S. Semiconductor-Based Photocatalytic Hydrogen Generation. *Chem. Rev.* **2010**, *110*, 6503–6570.

(48) Watanabe, H.; Fujikata, K.; Oaki, Y.; Imai, H. Band-Gap Expansion of Tungsten Oxide Quantum Dots Synthesized in Sub-Nano Porous Silica. *Chem. Commun.* **2013**, *49*, 8477–8479.